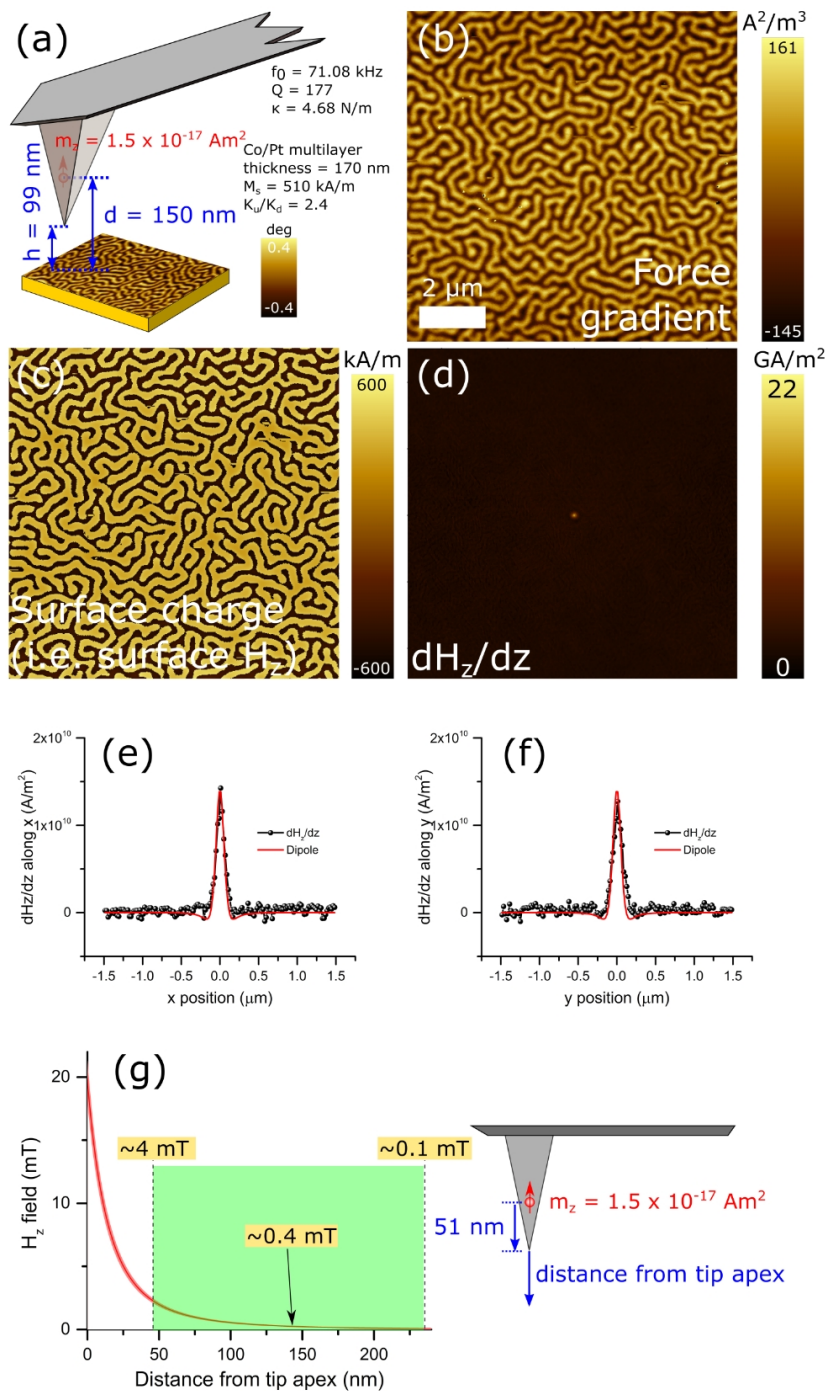
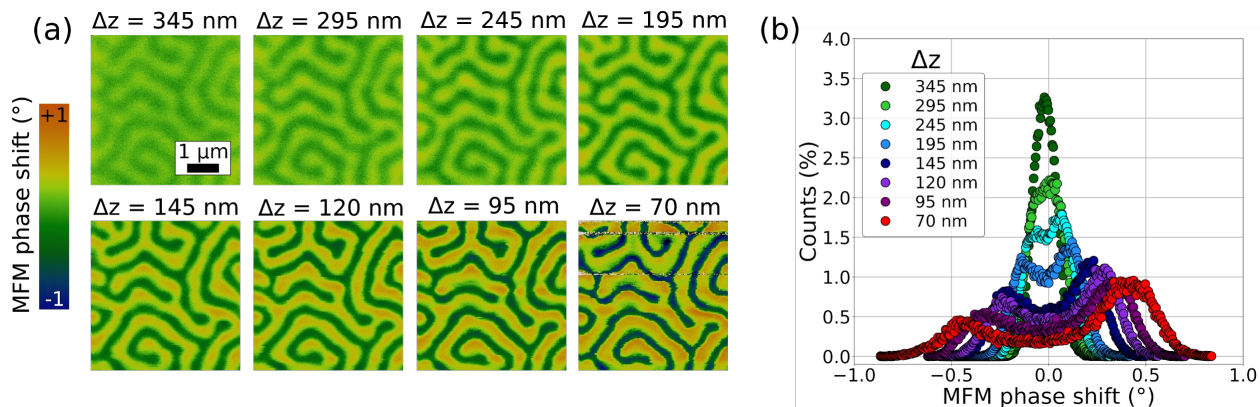


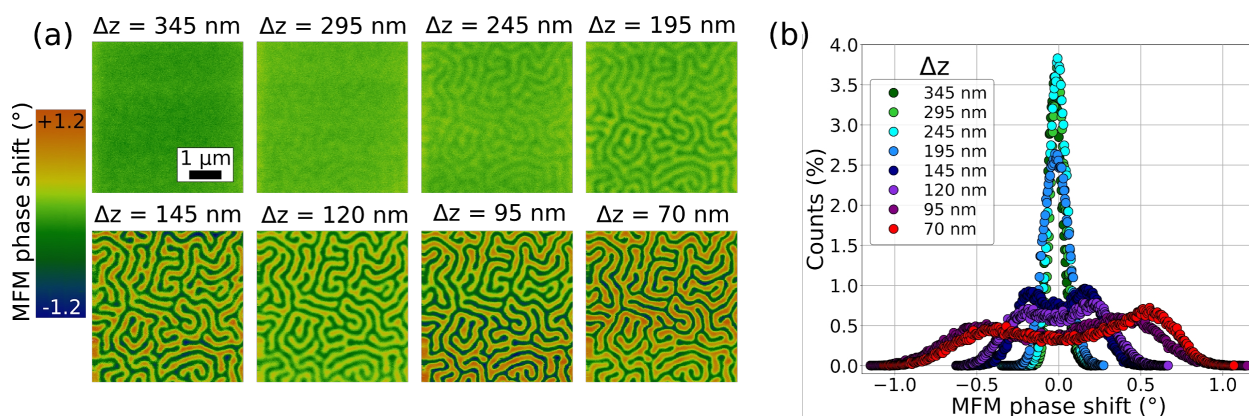
SUPPLEMENTARY FIGURES



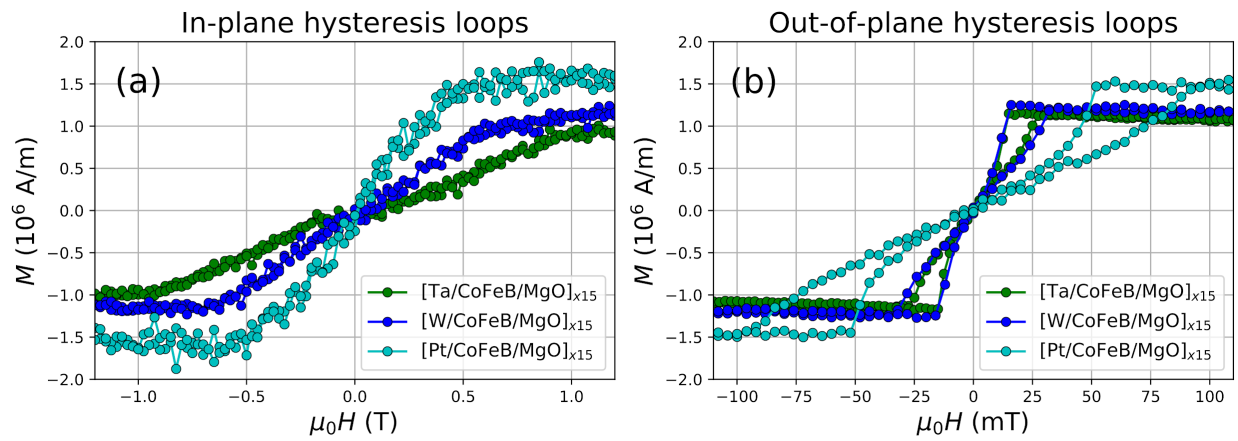
Supplementary Figure 1. Measurement of the MFM probe stray field. (a) Schematic representation of the probe during the second pass while performing MFM imaging. (b) MFM phase image converted to force gradient using probe mechanical properties. (c) Sample surface charge reconstructed from (b) using material parameters. (d) RSTTF (i.e. gradient of the magnetic field generated by the probe). (e) and (f) cross sections taken from (d) along with the field gradient from a dipole. (g) Z-component of the magnetic field generated by the magnetic dipole along with schematic representation of the dipole position in respect to the probe apex. The distance from the tip apex coincides with the tip lift height Δz in the main text. The green shaded area in the graph represents a probe oscillation of 200 nm peak-to-peak.



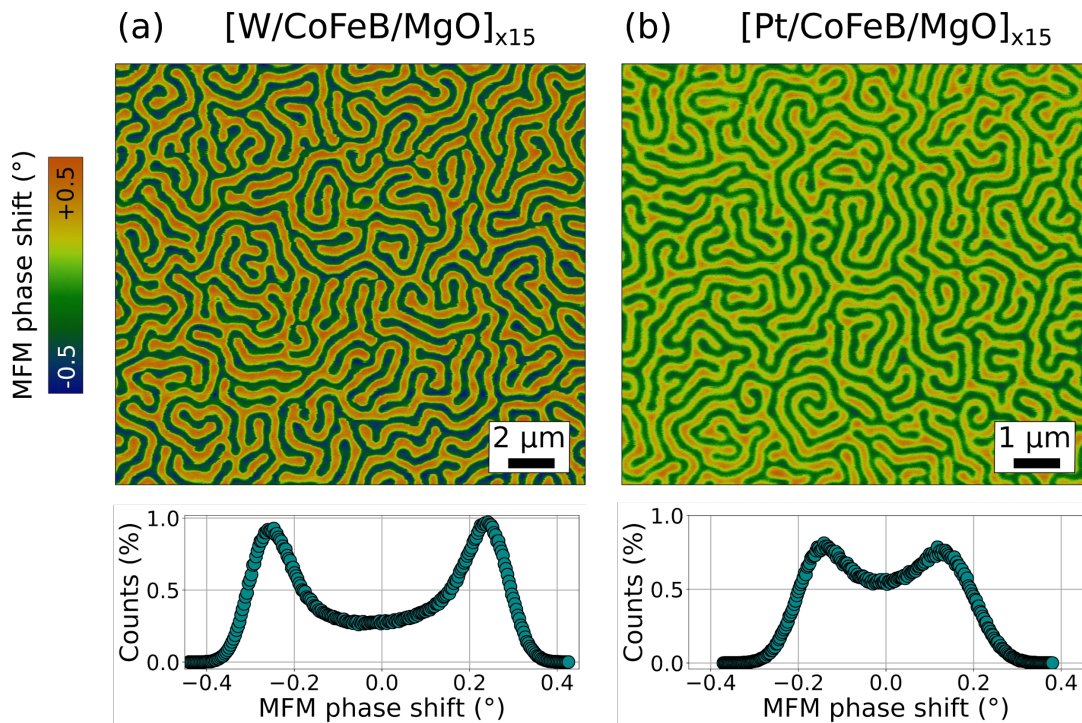
Supplementary Figure 2. MFM image perturbations caused by probe-sample magnetic interaction on the W/CoFeB/MgO multilayer. (a) MFM imaging of the demagnetised state of W/CoFeB/MgO multilayer at different tip lift height Δz , with the corresponding image histograms shown in (b). The bin width is kept constant across all histograms.



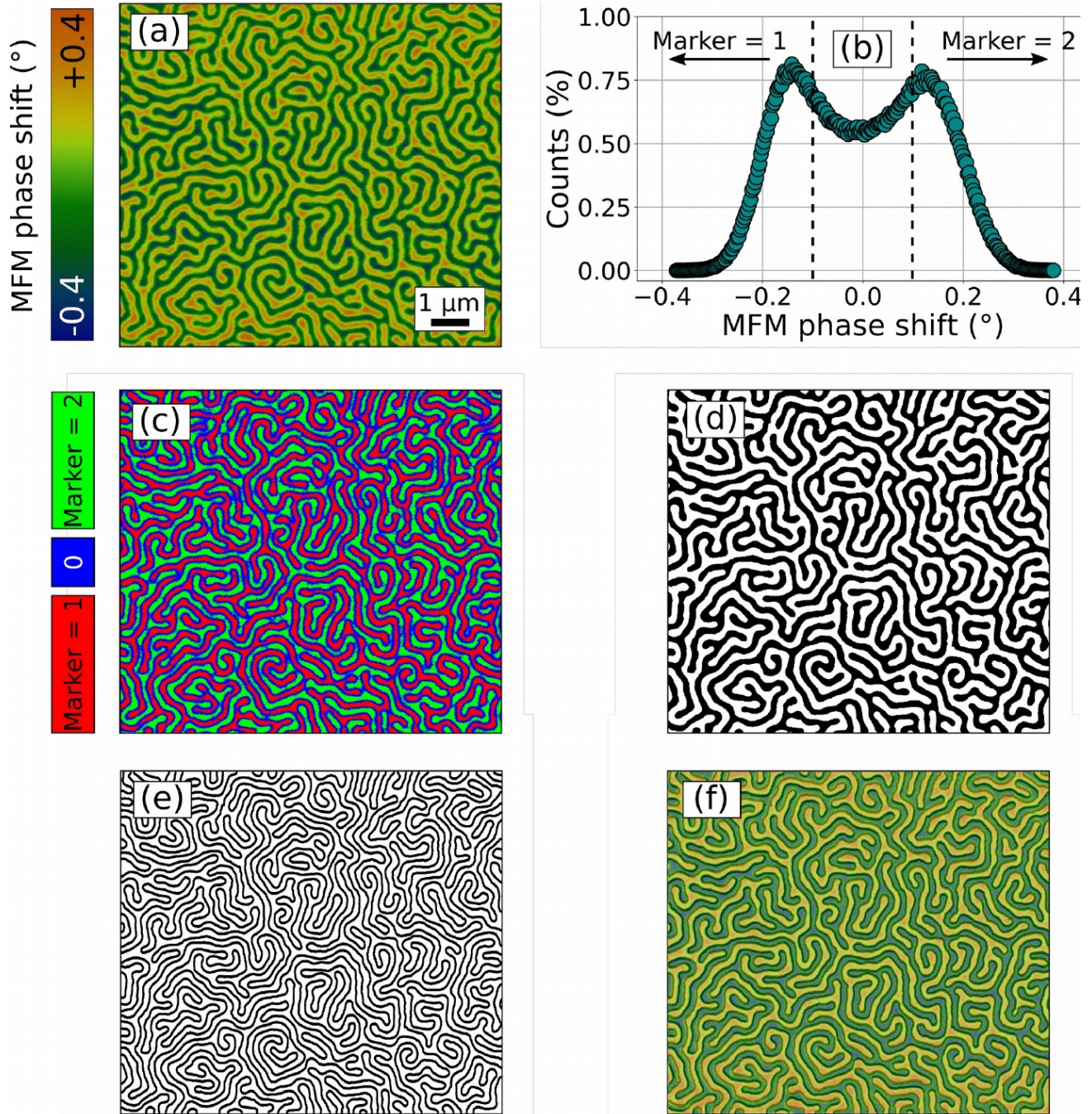
Supplementary Figure 3. MFM image perturbations caused by probe-sample magnetic interaction on the Pt/CoFeB/MgO multilayer. (a) MFM imaging of the demagnetised state of Pt/CoFeB/MgO multilayer at different tip lift height Δz , with the corresponding image histograms shown in (b). The bin width is kept constant across all histograms.



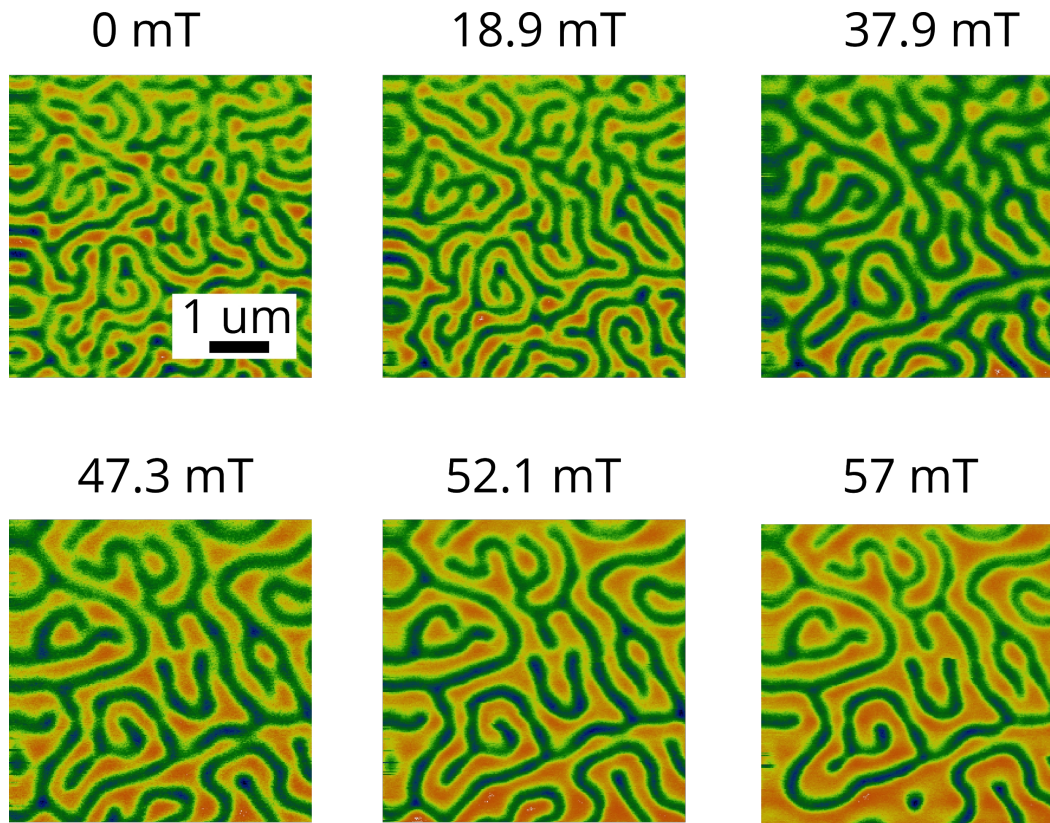
Supplementary Figure 4. Magnetic hysteresis loops measured by VSM magnetometry at room temperature. In-plane (a) and out-of-plane (b) magnetic hysteresis loops measured by VSM magnetometry for all samples investigated: [Ta/CoFeB/MgO]_{x15}, [W/CoFeB/MgO]_{x15}, and [Pt/CoFeB/MgO]_{x15}. The values of saturation magnetisation M_s and effective anisotropy constant K_{eff} listed in Tab. 1 are extracted from these loops. The values of perpendicular saturation field quoted in the main text (i.e. 27 mT, 36 mT, and 94 mT for Ta-, W-, and Pt-based stacks, respectively) are also extracted from these loops and are consistent with the values measured locally by MFM imaging: 25 mT, 37 mT and 85 mT, respectively.



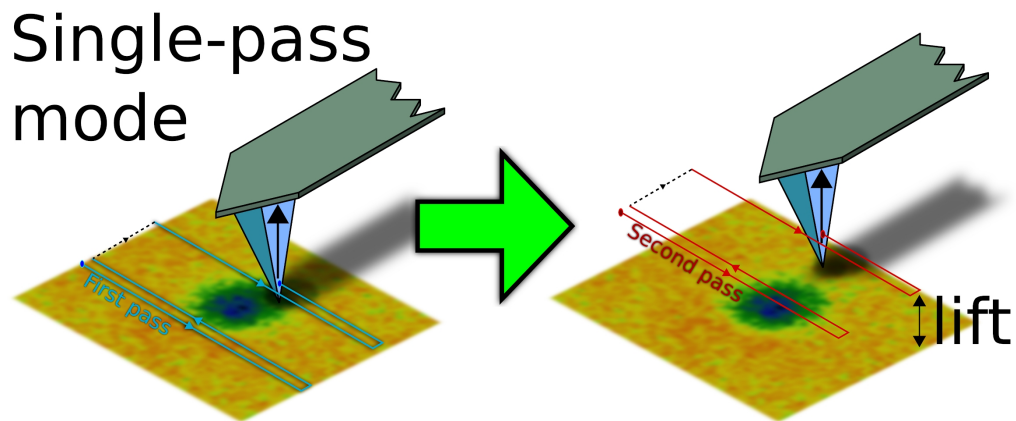
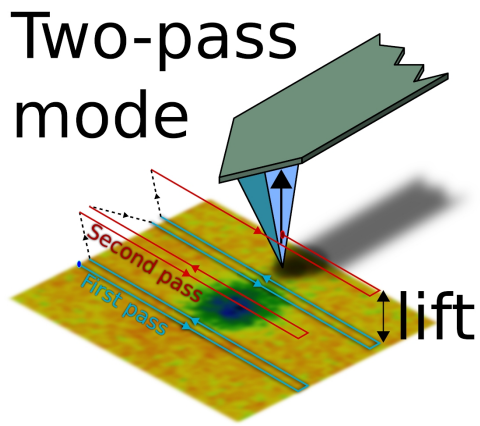
Supplementary Figure 5. MFM images of the demagnetised state for W/CoFeB/MgO and Pt/CoFeB/MgO multilayers. MFM images of the demagnetised state for (a) W/CoFeB/MgO and (b) Pt/CoFeB/MgO multilayers, with the corresponding image histograms also shown. The lift height used during second pass is $\Delta z = 125$ nm and 115 nm, respectively. A small out-of-plane bias field is applied during imaging to compensate for the tip-induced perturbations.



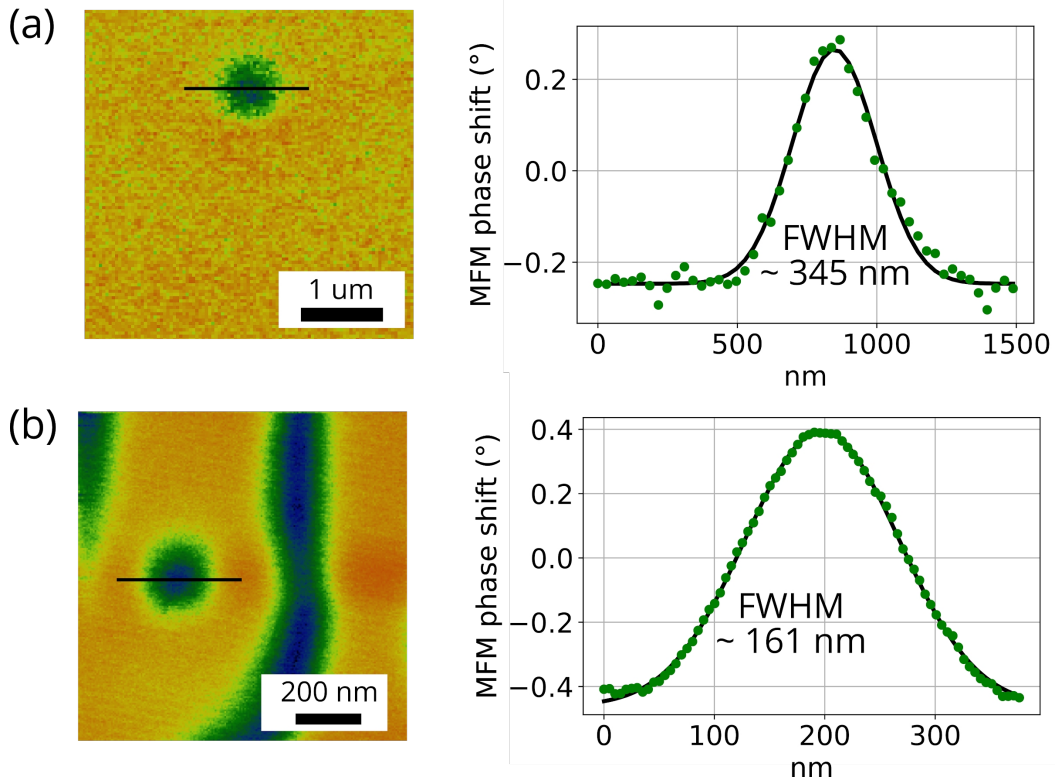
Supplementary Figure 6. Procedure used to measure the average equilibrium domain width through a random walker segmentation process. (a) Original MFM image of the demagnetised state for Pt/CoFeB/MgO multilayer. (b) Corresponding image histogram. The dashed lines indicate the values of the MFM phase shift below or above which markers are set to 1 and 2, respectively. (c) Marker values illustrated pixel by pixel. (d) Result of the random walker segmentation algorithm applied to (a) with the choice for markers as in (b). The areas of black and white domains cover 50.1% and 49.9%, respectively, of the whole image. (e) Contours of the domains extracted from (d). (f) Overlap between (a) and (e) illustrating the good match of the detected domain edges to the imaged magnetic domains.



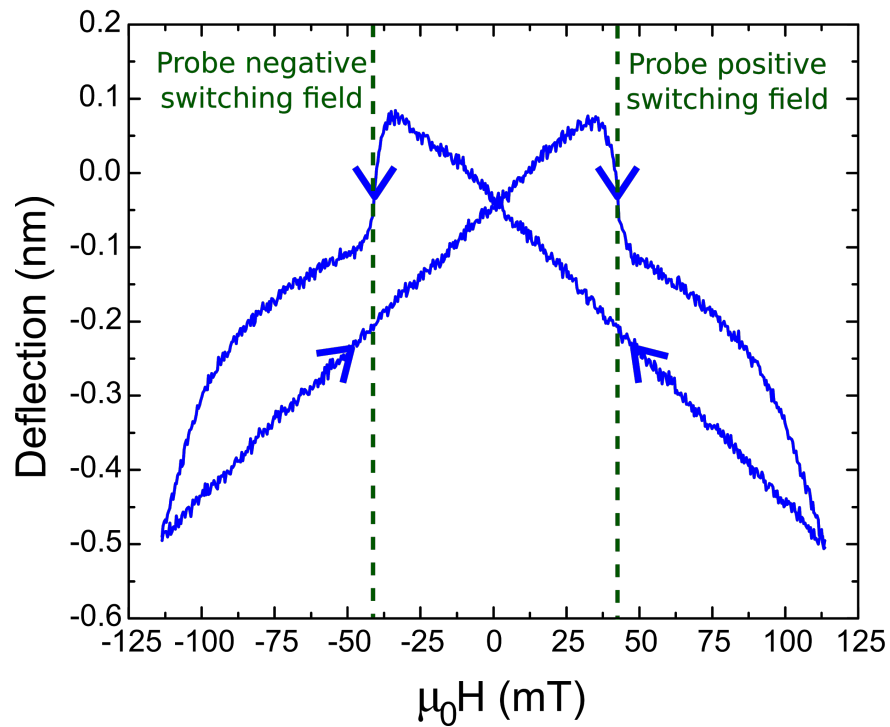
Supplementary Figure 7. Imaging of skyrmion nucleation with increasing field in Pt/CoFeB/MgO. MFM images acquired in single pass mode illustrating the process of skyrmion nucleation from the shrinking of stripe domains upon increasing applied perpendicular field H_z . The lift height is $\Delta z = 145$ nm. All images are based on a reference topography that was acquired in zero applied field. Note that one individual skyrmion is nucleated at $H_z = 57$ mT.



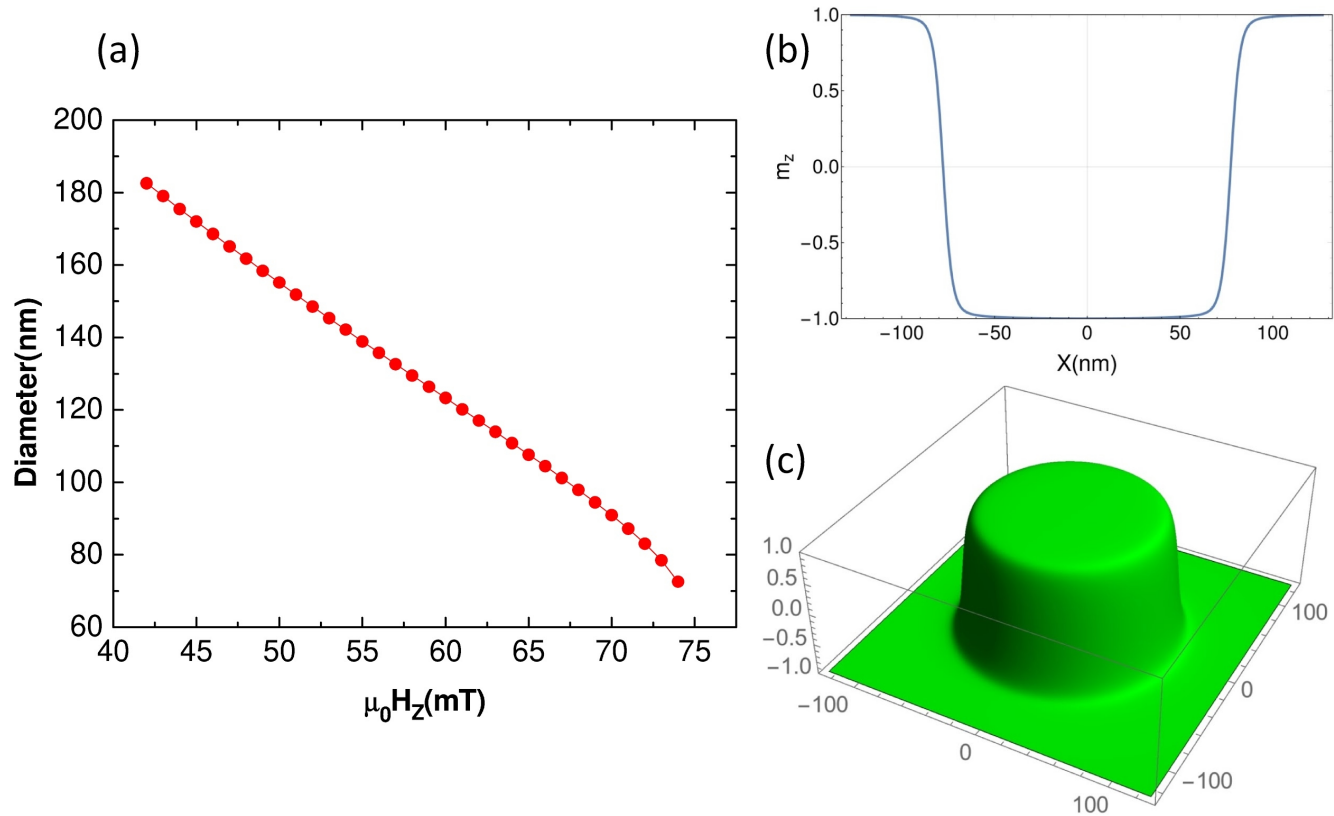
Supplementary Figure 8. Difference between two-pass and single-pass MFM modes. In two-pass MFM mode, topography (first pass) and phase signal (second pass) are acquired at each line scan. On the other hand, in single-pass mode, topography and phase signal are acquired separately for the desired sample area. In both modes topography scans are performed with the tip as close as possible to the sample surface, while phase scans are performed at a set lift height.



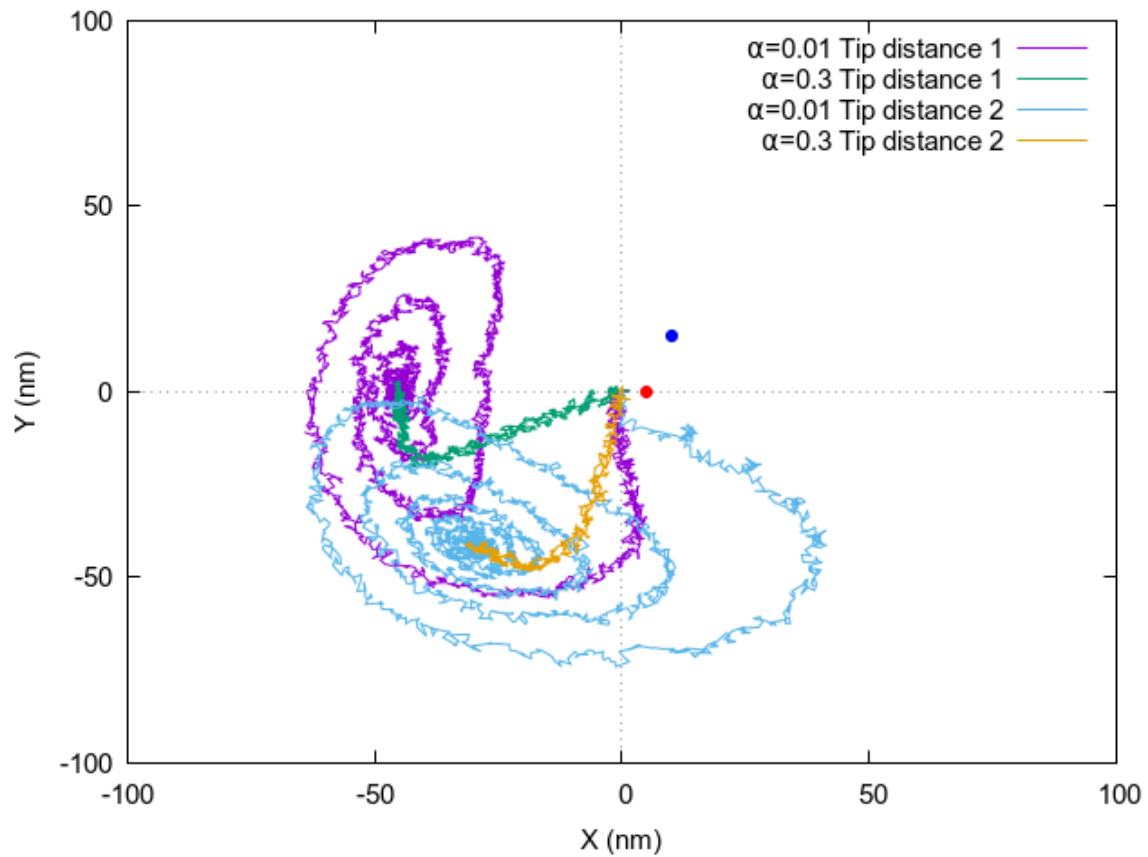
Supplementary Figure 9. Upper limit of skyrmion diameter. Single pass MFM images of individual skyrmions in (a) W/CoFeB/MgO and (b) Pt/CoFeB/MgO multilayers. Both images are taken at a lift height $\Delta z = 145$ nm and under an applied perpendicular field of 32 mT and 57 mT, respectively. The black lines in the skyrmion images are the linescans across which the skyrmion size is measured. The Full Width at Half Maximum (FWHM) is 345 nm and 161 nm, respectively. We note that this is only an upper bound to the actual skyrmion size, which could not be exactly measured due to impossibility to determine the deconvolving TTF, as explained in Supplementary Note 3.



Supplementary Figure 10. Magnetic switching field of the MFM probe. The MFM cantilever is kept at a constant height, 500 micrometers above the perpendicular magnet, while the magnetic field is swept between -113 mT and +113 mT and the deflection of the cantilever is measured. Plotting cantilever deflection as a function of applied magnetic field, allows to identify the probe switching field via the two abrupt jumps in deflection (one at negative and one at positive fields), as marked by the dashed vertical lines. The switching field of this particular probe is $\sim \pm 42$ mT, meaning that for applied fields higher than +42 mT (or lower than -42 mT), the tip magnetisation is always aligned along the field direction.



Supplementary Figure 11. Micromagnetic simulations of the skyrmion configurations. The skyrmion configuration has been calculated for the parameters corresponding to Pt/CoFeB/MgO using the effective medium model. (a) Diameter of the skyrmion as a function of the applied field. (b) Magnetization Skyrmion profile as a function of the distance for an applied field of 50 mT. (c) Three dimensional profile of the skyrmion for an applied field of 50 mT. For visualization purposes, the third component of the magnetization has been inverted.



Supplementary Figure 12. Micromagnetic simulations of the skyrmion trajectories. Simulated trajectories of the skyrmion center under the effect of the dipole field for an applied field perpendicular to the film plane of 50 mT. To illustrate the gyrotropic character of the motion two different damping parameters and two tip positions are analyzed. The initial position of the skyrmion is at the center of coordinates. The distance from the dipole to the surface of the sample is 98 nm and the dipole magnitude is $m_z = 8.8 \times 10^{-17} \text{ A m}^2$. The in-plane positions of the dipole are (5nm,0) for tip distance 1 (red dot) and (10 nm, 15nm) for tip distance 2 (blue dot).

SUPPLEMENTARY NOTES

Supplementary Note 1. Measurement of the MFM probe stray field

A magnetic probe from the same model used in the main text (i.e. NT-MDT Low Moment / Tips Nano Low Moment) has been calibrated using the tip transfer method [1-7]. The measured mechanical properties of the tip were: resonant frequency $f_0 = 71.08$ kHz (standard deviation 0.2 kHz), quality factor $Q = 177$ (standard deviation 10), and spring constant $k = 4.68$ N/m (standard deviation 0.07 N/m).

To perform the tip transfer method, a reference sample composed of Co/Pt layers (thickness 170 nm), was imaged using standard two pass MFM imaging (see Supplementary Figure 1(a)) at 512 by 512 pixels with pixel size 19.53 nm. The phase image obtained was then converted into force gradient using the mechanical properties of the probe (see Supplementary Figure 1(b)). Then, using Gwyddion software [8], the surface magnetic charge was calculated from the force gradient (see Supplementary Figure 1(c)). From the force gradient and the surface charge, the real space tip transfer function (RSTTF), i.e. z derivative of the z component of the stray magnetic field from the probe, was then calculated (see Supplementary Figure 1(d)).

The stray magnetic field values from the probe were then estimated approximating the field from the probe by that of a magnetic dipole (see Eq. 1):

$$H = \frac{1}{4\pi} \left(\frac{3r(m \cdot r)}{r^5} - \frac{m}{r^3} \right) \quad (\text{Eq. 1})$$

Where m is the magnetic dipole vector and r is the position assuming the dipole is at the origin. Taking the derivative along the z -direction (i.e. vertical) Eq. 1 turns into Eq. 2:

$$\frac{dH_z}{dz} = \frac{1}{4\pi} \left(3 \frac{m \cdot r}{r^5} + 6 \frac{m_z r_z}{r^5} - 15 r_z^2 \frac{m \cdot r}{r^7} \right) \quad (\text{Eq. 2})$$

The plots in Supplementary Figures 1(e) and 1(f) compare cross sections of the RSTTF, along the x and y directions respectively, with the numerical values from Eq. 2, assuming a magnetic dipole with z component only and value $m_z = 3.5 \times 10^{-17}$ Am², and a vertical distance of 150 nm (i.e. the 99 nm between the probe and the sample's surface plus 51 nm between the tip apex and the dipole position, as depicted in Supplementary Figure 1(g)).

By repeating the calibration process three times, using different areas of the Co/Pt reference sample, the average dipole value obtained is $m_z = 8.8 \times 10^{-17}$ Am² with a standard deviation of $m_z = 5.6 \times 10^{-17}$ Am². Using Eq. 1, this dipole approximation can be used to estimate the z -component of the magnetic field created from the probe, and how it decays with distance. The field from this average value, along with the fields from the maximum and minimum values obtained, can be seen in Supplementary Figure 1(g). This gives a field of 21 mT at the probe apex, and of ~ 0.4 mT at a distance of 140 nm from the tip apex (it is important to take into account that the probe's oscillation means that this value can be for instance as high as 4 mT if the oscillation amplitude is 200 nm peak-to-peak, hence making it consistent with the tip stray field value estimated at $\Delta z = 145$ nm quoted in

the main text). As a comparison, the field estimated for this probe is less than half the value reported for low moment probes from Bruker, ~ 57 mT [9].

Supplementary Note 2. Extraction of the average equilibrium domain width based on the random walker segmentation process

The random walker segmentation is a useful image processing algorithm that allows to precisely separate different phases in a noisy image. In our case, the two phases correspond to regions of an MFM image with magnetisation pointing out-of-the-plane, either up or down. As input parameters, the algorithm requires two markers, which label the 'certain' pixels of the two different phases in the image, respectively below and above set threshold values of grey levels of the image. For the 'uncertain' pixels in between these threshold values, the algorithm solves an anisotropic diffusion equation with tracers initiated at the 'certain' pixels positions, which have known marker value. The label of each unknown pixel is then attributed to the label of the known marker that has the highest probability to be reached first during the diffusion process [10].

An example of the application of the random walker segmentation algorithm to an MFM image of the Pt/CoFeB/MgO multilayer is presented in Supplementary Figure 2. The original demagnetised MFM image of the sample is shown in Supplementary Figure 2(a), with the corresponding histogram illustrated in Supplementary Figure 2(b). Here two markers are selected, respectively marker = 1 for values of MFM phase shift below -0.1° and marker = 2 for values of MFM phase shift above $+0.1^\circ$. This means that we label with certainty all pixels that have a gray level corresponding to a phase shift lower than -0.1° and higher than 0.1° as belonging to magnetisation pointing up or down, respectively. With this choice, the value of the markers for each image pixel is shown in Supplementary Figure 2(c), with red corresponding to marker = 1, light green corresponding to marker = 2, and blue representing the uncertain pixels (marker = 0) that typically lie at the edge between the two known regions, i.e. where the domain walls are. Supplementary Figure 2(d) illustrates the result of applying the random walker algorithm to the original image with the choice of the markers as discussed. The black and white regions represent the two well separated phases, or domains, with magnetisation pointing either up or down. Furthermore, from Supplementary Figure 2(d) it is easy to extract the contours of the magnetic domains (see Supplementary Figure 2(e)), which indeed match well the domains in the original image (see Supplementary Figure 2(f), which is an overlap of Supplementary Figure 2(a) and Supplementary Figure 2(e)).

The total area covered by each domain type is easily extracted from Supplementary Figure 2(d), by counting the number of pixels belonging to the black and white regions, respectively 50.1% and 49.9% in this case. The total length of all domain edges is also easily extracted from Supplementary Figure 2(e), by counting the pixels belonging to the contours. The average equilibrium domain width for each domain type is then calculated as the ratio between the area covered by each domain type and half of the total length of all domain edges.

Slight variations in the final average domain width are obtained depending on the choice of the threshold for the initial markers (see Supplementary Figure 2(b)), which is taken into account as an error. For the MFM image of the Pt/CoFeB/MgO multilayer presented in Supplementary Figure 2(a) the average equilibrium domain width obtained through this method is 179 ± 3 nm. The final value presented in Tab. 1 in the main text is different because it combines the image analysis procedure here discussed, with results obtained from using a standard 2-D fast Fourier transform (FFT).

Supplementary Note 3. Evaluation of skyrmion diameter

Images of individual skyrmions for W/CoFeB/MgO and Pt/CoFeB/MgO multilayers were acquired in single pass MFM mode and are illustrated in Supplementary Figures 9(a) and 8(b), respectively. From these images it is possible to extract an upper bound for the skyrmion diameter, which is given by the FWHM of the corresponding gaussian profile: FWHM ~ 345 nm and ~ 161 nm for W/CoFeB/MgO and Pt/CoFeB/MgO samples, respectively. In order to extract the real skyrmion diameter the TTF has to be deconvoluted from the skyrmion images. However, the TTF is estimated by imaging the reference sample (as in Supplementary Note 1 for the two pass mode) in exactly the same conditions used to image the skyrmion, i.e. also in single pass mode. But in single pass mode it is intrinsically harder to keep a constant lift height above the whole sample area, since the reference topography scan for that same area was measured previously, up to an hour before for a high resolution image. It follows that even small drifts in the lift height during single pass prevent to extract a reliable TTF from the reference sample. Thus, the only information that we can provide is an upper limit for the skyrmion diameter.

The skyrmion diameter corresponding to the extracted DMI strength was anyhow calculated through micromagnetic simulations. We simulated the equilibrium configuration of the skyrmions using the micromagnetic code mumax3 [11]. For this evaluation, we considered the multilayer of Pt/CoFeB/MgO with 15 repetitions. The micromagnetic parameters are the experimental values as reported in Table 1 of the main body of the article. The used exchange constant is $A=10$ pJ/m. To simplify the calculation in the multilayers, we implemented the effective medium model [12,13]. In such a model, a repetition, comprising the nonmagnetic layers and the magnetic layer, is considered as a single magnetic layer with the thickness of the periodicity. All the magnetic parameters have to be rescaled according to the following relations:

$$A' = fA, D' = fD, M_s' = f M_s \text{ and } K_U' = f K_U - \frac{\mu_0 M_s^2}{2} (f - f^2) \quad (\text{Eq. 3})$$

where $f = t_m/t_{rep}$ is the ratio between the thickness of the magnetic layer t_m and the thickness of the repeated layer t_{rep} . For the Pt/CoFeB/MgO multilayers, $t_m = 0.8$ nm, $t_{rep} = 5.6$ nm and $f = 0.1428$. The advantage of such a simplification is to avoid the discretization of the non magnetic layers. With such an approach, the discretization size is $2 \times 2 \times 5.6$ nm³. The simulated grid is $512 \times 512 \times 15$ and the size of the simulated sample is $1024 \times 1024 \times 84$ nm³. We used a cell for each layer because in the dynamic simulations we have to include the dipole field, which varies along the thickness of the multilayer. Supplementary Figure 11(a) presents the simulated skyrmion diameter as a function of the applied field. The simulations present a reasonable agreement regarding the skyrmion radius and range of fields of existence of the skyrmion with respect to the experimental results. To illustrate the skyrmion character, the profiles obtained for a field of 50 mT in the simulation are plotted in Supplementary Figure 11(b) and (c).

Supplementary Note 4. Micromagnetic simulations of the skyrmion dynamics under a magnetic dipole

To illustrate the skyrmion dynamics under the influence of the tip, we included the magnetic field created by the dipole given by Eq. 1 in the dynamic micromagnetic simulations. To understand and analyze such a motion is better to introduce the Thiele equation [14]. This approach considers the skyrmion to have a rigid shape whose center can be characterized with coordinates $\vec{R}=\{X, Y\}$. The external field created by the dipole contributes with the force term \vec{F} . This force is zero for constant fields but is non zero under field gradients, as the field created by a dipole. For our system:

$$\vec{G} \times \dot{\vec{R}} - \alpha \tilde{D} \dot{\vec{R}} + \vec{F}(\vec{R}) = 0 \quad (\text{Eq. 4})$$

where \vec{G} is the gyrotropic vector, \tilde{D} is the dissipation dyadic, α is the Gilbert damping and \vec{F} is the external force. The dipole field has radial symmetry and, therefore, the force created by the dipole is central and its magnitude is only a function of the radius. The Skyrmion Hall Angle θ_{SHA} [15] in this case can be simplified as:

$$\tan \theta_{SHA} = v_{\phi} / v_r = \frac{G_z}{\alpha D} \quad (\text{Eq. 5})$$

where v_r is the radial component of the skyrmion velocity, v_{ϕ} is the azimuthal component, G_z is the third component of the gyrotropic vector and D is the diagonal element of the dissipation dyadic. The dipole produces a force along the radial component but the gyrotropic term creates an azimuthal component of the speed. G_z is proportional to the skyrmion number and, thus, also the deflection angle is. The skyrmion number in our simulations is equal to -1. Differently from the current-induced skyrmion motion [15], this deflection angle has radial symmetry, is not constant and depends on the actual position. The Thiele equation is only a first approximation because the dipole field will produce changes to the skyrmion profile. To study the dynamics, micromagnetic simulations have to be performed. Supplementary Figure 12 shows the trajectory for two different dipole positions and two different damping parameters. Those damping parameters correspond to typical values for large and small damping in perpendicular materials. As initial configuration we take the configuration calculated in Supplementary Note 3 and introduce the field created by a dipole at a vertical distance of 98 nm from the sample surface. The dipole is oriented along z with a magnitude $m_z = 8.8 \times 10^{-17} \text{ A m}^2$. The in-plane position of the dipole are (5nm,0) for tip distance 1 and (10 nm, 15nm) for tip distance 2. We start with the skyrmion at the center of the sample and consider the tip off centered. After some interval of time the skyrmion stops, corresponding to a situation where in the Thiele equation the force is zero. This position depends on the tip distance from the sample. The skyrmion trajectory appears to have some stochastic features but in reality that corresponds to the excitation of the internal modes of the skyrmion. Those modes are excited due to the inhomogeneous field created by the dipole and the possibility

of variations of the skyrmion profile along the sample thickness. In first approximation, such excitations can not be modeled with the Thiele equation. The trajectories are in agreement with the role of the damping. Larger damping corresponds to a less deflected trajectory in agreement with the Skyrmion Hall Angle equation and as it can be verified in the trajectories presented in Supplementary Figure 12. To summarise, the tip will produce a net displacement of the skyrmion in the radial direction.

SUPPLEMENTARY REFERENCES

1. Hug, H. J. *et al.* Quantitative magnetic force microscopy on perpendicularly magnetized samples. *J. Appl. Phys.* **83**, 5609 (1998).
2. Vock S., *et al.* Quantitative magnetic force microscopy study of the diameter evolution of bubble domains in a (Co/Pd)₈₀ multilayer, *IEEE Trans. Magn.* **47**, 2352 (2011).
3. Vock S, *et al.* Magnetic vortex observation in FeCo nanowires by quantitative magnetic force microscopy, *Appl. Phys. Lett.* **105**, 172409 (2014).
4. Vock, S. Resolving local magnetization structures by quantitative magnetic force microscopy. (Technischen Universitat Dresden, 2014).
5. Reiche, C. F. *et al.* Bidirectional quantitative force gradient microscopy. *New J. Phys.* **17**, 013014 (2015).
6. Puttock, R. *et al.* V-shaped domain wall probes for calibrated magnetic force microscopy, *IEEE Trans. Magn.* **53**, 1-5 (2017).
7. Panchal, V. *et al.* Calibration of multi-layered probes with low/high magnetic moments, *Sci. Rep.* **7**, 7224 (2017).
8. Nečas, D. and Klapetek, P. Gwyddion: an open-source software for SPM data analysis, *Open Phys.* **10**, 181 (2012).
9. Zhang, S. *et al.* Direct writing of room temperature and zero field skyrmion lattices by a scanning local magnetic field, *Appl. Phys. Lett.* **112**, 132405 (2018).
10. Grady, L. Random walks for image segmentation, *IEEE Trans. Pattern Anal. Mach. Intell.* **28**, 1768 (2006).
11. Vansteenkiste, A. *et al.* The design and verification of MuMax3, *AIP Adv.* **4**, 107133 (2014).
12. Woo, S. *et al.* Observation of room-temperature magnetic skyrmions and their current-driven dynamics in ultrathin metallic ferromagnets, *Nat. Mater.* **15**, 501 (2016).
13. Lemesh, I. *et al.* Accurate model of the stripe domain phase of perpendicularly magnetized multilayers, *Phys. Rev. B* **95**, 174423 (2017).
14. Thiele, A.A. Steady-State Motion of Magnetic Domains, *Phys. Rev. Lett.* **30**, 230 (1973).
15. Jiang, W. *et al.* Direct observation of the skyrmion Hall effect, *Nat. Phys.* **13**, 162 (2017).